In Situ Observation of Nanoparticle Exsolution from Perovskite Oxides; from Atomic Scale Mechanistic Insight to Nanostructure Tailoring

Dragos Neagu[1], Vasileios Kyriakou[2], Ioan-Lucian Roiban[3], Mimoun Aouine[4], Chenyang Tang[1], Angel Caravaca[3], Kalliopi Kousi[1], Ingeborg Schreur-Piet[5], Ian S. Metcalfe[1], Philippe Vernoux[3], Mauritius C.M. van de Sanden[2,6] and Mihalis N. Tsampas[2]**

(1) Newcastle University, School of Engineering, NE1 7RU, UK

(2) Dutch Institute for Fundamental Energy Research (DIFFER), 5612 AJ Eindhoven, the Netherlands

(3) Univ Lyon, Insa-Lyon, Université Claude Bernard Lyon I, CNRS UMR 5510, Mateis, 7 av Jean Capelle, 69621 Villeurbanne Cedex, France

(4) Univ. Lyon, Université Claude Bernard Lyon 1, CNRS - UMR 5256, IRCELYON, 2 avenue A. Einstein, 69626 Villeurbanne, France

(5) Department of Chemical Engineering & Chemistry, Eindhoven University of Technology, 5600 MB Eindhoven, The Netherlands

(6) Department of Applied Physics, Eindhoven University of Technology, 5600 MB Eindhoven, the Netherlands

ABSTRACT: Understanding and controlling the formation of nanoparticles at the surface of functional oxide supports is critical for tuning activity and stability for catalytic and energy conversion applications. Here we use a latest generation environmental transmission electron microscope to follow the exsolution of individual nanoparticles at the surface of perovskite oxides, with ultra-high spatial and temporal resolution. Qualitative and quantitative analysis of the data reveals the atomic scale processes that underpin the formation of the socketed, strain-inducing interface that confers exsolved particles their exceptional stability and reactivity. This insight also enabled us to discover that the shape of exsolved particles can be controlled by changing the atmosphere in which exsolution is carried out and additionally, this could also produce intriguing heterostructures consisting of metal-metal oxide coupled nanoparticles. Our results not only provide insight into the *in situ* formation of nanoparticles, but also demonstrate the tailoring of nanostructures and nano-interfaces.

KEYWORDS: nanoparticles, *in situ* exsolution, perovskites, environmental transmission electron microscopy, nanostructuring

Functional materials consisting of metallic particles dispersed on the surface of oxides have been instrumental in enabling various catalytic and energy conversion applications.[1–3] For the last decades, such materials have been generally prepared by deposition methods whereby catalyst precursors are deposited over the surface of the oxide support, followed by various thermal

decomposition or reduction processes to form the metallic nanoparticles. In the last decade, an alternative preparation route has emerged whereby the catalyst in its ionic form is substituted into the crystal lattice of an oxide support under oxidising conditions and subsequently released as metallic nanoparticles at the surface, upon reduction at temperature (Fig. 1). This process has been referred to as solid state recrystallisation[4] or intelligent self-regeneration[5] when carried out in a reversible manner, and as redox exsolution[6] when particle release at the surface is irreversible.

As compared to particles prepared by deposition methods which usually form relatively shallow interfaces with the oxide support, exsolved particles are not only more uniformly dispersed but are also partly immersed (or socketed) into the surface of the host oxide support.[7] In turn, this makes them considerably better anchored and more resistant to degradation by agglomeration or carbon deposition, and, at the same time, strained, which provides opportunities for accessing higher catalytic activity.[7,8] Therefore, exsolution has emerged as an exciting platform for the design of advanced nanostructures, unlocking additional levels of reactivity and stability for various applications including fuel cells,[9–13] H_2O, CO_2 and/or CH_4 (co)electrolysis,[14–19] chemical looping H_2 production,[20] membrane reactors[21] and catalysis of CO and NO oxidation,[8] CO_2 reduction,[22] photocatalysis[23] and hydrocarbon reforming.[24–26]

So far, several aspects of the exsolution mechanism have been investigated aiming to understand the factors that control the size, population[27,28] and energetics of particle formation,[29–32] as well as the role of defects within the perovskite host lattice.[6,33–35] However, the formation of the defining structural aspect of exsolved particles – their socketed, epitaxial interface with host oxide – remains difficult to understand due to the challenges of observing atomic scale processes with sufficiently high spatial and temporal resolution. Understanding their genesis would not only allow

further tuning of their functionality, such as stability and reactivity, but could also provide insights for creating advanced interfaces with superior functionality.

Here we use a latest generation environmental transmission microscope to capture the exsolution dynamics of individual nanoparticles with ultra-high spatial and temporal resolution. This allowed us to reveal and describe quantitatively the atomic scale processes that underpin the formation of the distinctive particle-host lattice interface as well as the stepwise, discrete nature of particle growth which seems to correlate with the highly uniform manner in which exsolved particles emerge. Additionally, the results also provide proof of concept for controlling the exsolution process to create advanced nanostructures.

RESULTS AND DISCUSSION

The challenges of observing exsolution *in situ*. To follow the dynamics of nanoparticle exsolution, we select two compositions with vastly different content of exsolvable ions (x = 0.06 and 0.4 in $A_{1-\alpha}B_{1-x}M_xO_3$), to cover the currently reported range of exsolved structures and applications. The sample with a relatively low content of exsolvable Ni ions is $La_{0.43}Ca_{0.37}Ni_{0.06}Ti_{0.94}O_3$,[15] while the one with relatively high content is $La_{0.8}Ce_{0.1}Ni_{0.4}Ti_{0.6}O_3$.[6] The relative content of exsolvable ions in the perovskite crystal lattice can be visually compared in Fig. 1. We employ these samples in powder or lamella form, as detailed later in the text.

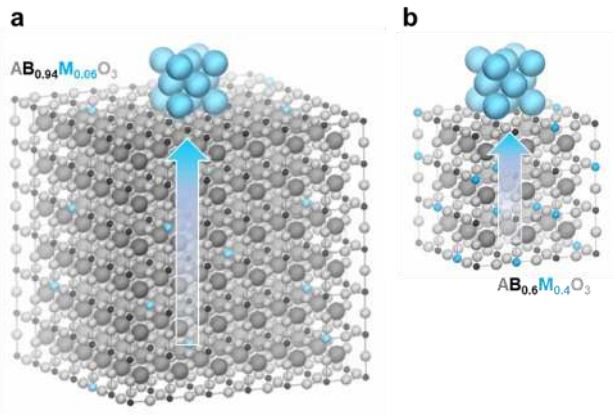

Figure 1. Exsolution from perovskites with different substitution level. Illustration of the number of perovskite unit cells required to form one metal unit cell (14 metal atoms) from perovskites $A_{1-\alpha}B_{1-x}M_xO_3$ with substitution of M: (a) x = 0.06 (6x6x6 cells), (b) x = 0.4 (3x3x3 cells).

Exsolved particles, as required by various applications, are grown routinely in the size range of 5-50 nm.[2] To monitor their growth, one would have to use imaging techniques suitable for this scale, such as electron microscopy. Transmission electron microscopy (TEM), in particular, has the advantage of reaching an atomic-scale spatial resolution in the recorded image by passing an electron beam though a small area of the sample, thus providing a "see-through" image of the particle, the host oxide and their interface, at the same time. However, in order to obtain an image, the region analysed needs to be thin-enough, that is, "electron-transparent" (usually at the edge of grains, Fig. 2a) and preferably oriented along a major crystallographic axis to facilitate data interpretation. Carrying out TEM imagining under gas environment and at temperature brings additional challenges in terms of maintaining resolution and avoiding sample drift and misalignment due to thermal effects upon heating.[36] To address the above, we employed a latest generation FEI TITAN G2 80–300 kV environmental transmission electron microscope (ETEM) equipped with an objective Cs aberration corrector and equipped with a double tilt holder, which

can operate under gas pressure up to at 20 mbar and temperatures up to 1300 °C.[37,38] To minimise thermal drift upon heating up we secure the samples on high-performance DENSolutions nano-chips. The instrument is capable of continuous recording of video files at 4K pixel resolution at a spatial resolution of 0.09 nm in TEM mode and at a rate of 20-30 frames per second equivalent to a time resolution of ~50 ms.

Particle-perovskite socket formation. To obtain information on the formation of the particle-socket interface in conditions representative for a wide range of applications, we used a powder sample of $La_{0.43}Ca_{0.37}Ni_{0.06}Ti_{0.94}O_3$, under a H_2 atmosphere (20 mbar), at 900 ºC. We then followed the structural evolution of different areas across the edge of a perovskite grain (Fig. 2a,b), over the first few minutes of particle growth which are considered to be the defining moments in the genesis of exsolved particles and their distinctive characteristics, as well as being the most difficult to investigate. Fig. 2c shows the time evolution of a representative area over 250 s, while Fig. 2d-g plots corresponding particle and perovskite dimensions of interest extracted from these data. Due to the very fast nature of the exolution process and due to the difficulty of anticipating the location where a particle would nucleate, we were unable to capture the very first moments of nucleation. At the time labelled as t = 0 s the particle appears to have nucleated instantaneously, displaying an approximate apparent height and width of 1 and 3 nm, and growing to 1.7 and 4.5 nm, respectively, by t = 250 s. Interestingly, most of the particle growth occurs in under 100 s suggesting that short reduction times and/or reduction pulses might be sufficient to tailor exsolved particles as compared to the relatively long reduction times typically used in the literature, which are of the order of hours. However, it should also be noted that this result is consistent with a previous report indicating that exsolved particles can be formed *via* electrochemical reduction in just a few tens of seconds.[15] Particle growth is not only fast, but also apparently isotropic, that is, dimensionally the

particle grows proportionally in all directions, as evidenced by a plot of a particle height as a function of corresponding width (Fig. 2e). Additionally, throughout the growth process, the particle remains locked in close crystallographic orientation (in [110] direction) with respect to the perovskite lattice, which is one of the key structural elements that confers exsolved particles their stability.

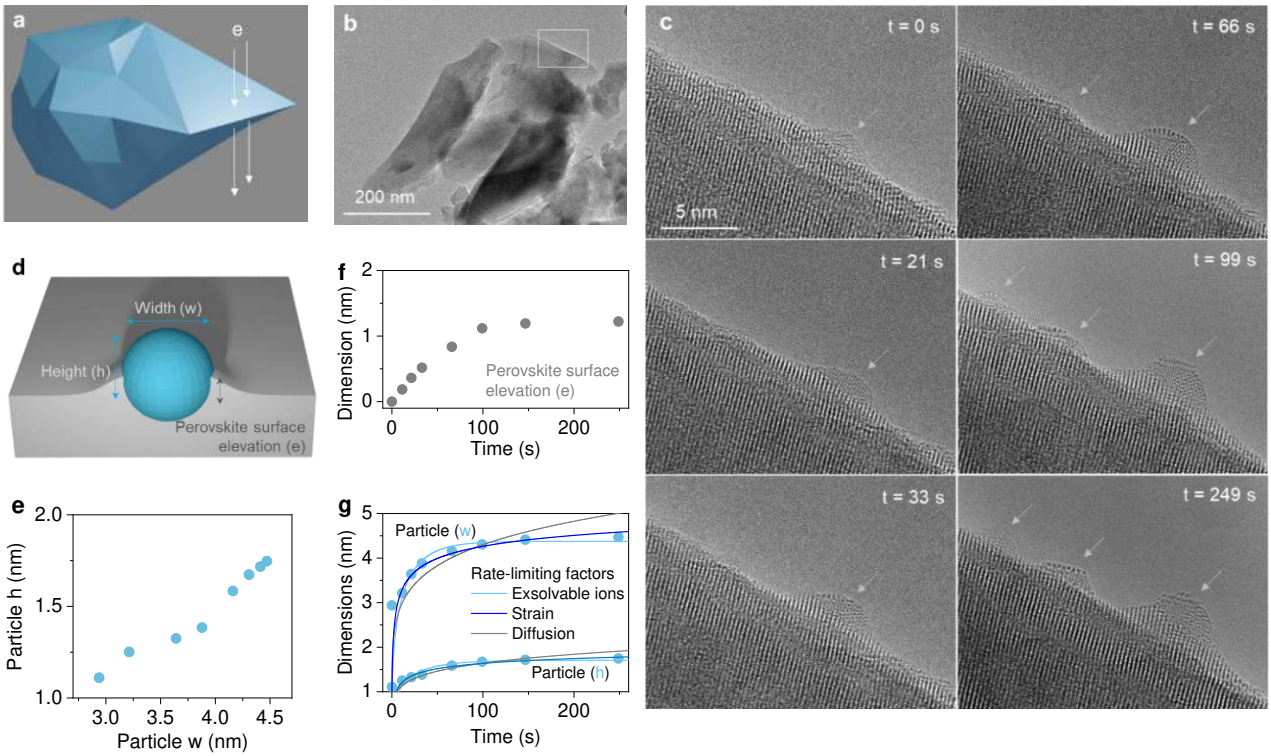

Figure 2. Particle-socket formation during *in situ* growth under H_2. (**a**) Schematic illustration of a perovskite particle in a suitable orientation for monitoring one of its edges by electron microscopy imaging. (**b**) TEM of a $La_{0.43}Ca_{0.37}Ni_{0.06}Ti_{0.94}O_3$ perovskite powder highlighting an edge of a grain where particle growth was followed. (**c**) Selected region followed throughout the reduction process at 900 °C, under H_2, showing snapshots at different times (t) of the gradual formation of a particle-socket and nucleation of two additional particles. (**d**) Schematic illustration of a particle within socket annotated with the dimensions used to quantify its evolution over time. (**e**) Plot of the

particle height vs width. (**f**) Plot of the elevation of the perovskite lattice in the region adjacent to the particle, as a function of time. (**g**) Plot of the particle width and height as a function of time together with various models identifying the rate-limiting step in particle growth.

One subtle, yet intriguing structural aspect that develops as the particle grows, is the evolution of the perovskite lattice around the particle. At t = 0 s, the surface of the perovskite lattice is seemingly flat. However, as the particle grows, the perovskite lattice rises concomitantly at the point of junction with the particle (see annotations in Fig. 2d and a plot of the values in Fig. 2f). This becomes apparent at around t = 33 s when the elevation of the perovskite lattice relative to the starting level (at t = 0 s) reaches about 0.3 nm and becomes clearly defined by t = 99 s, when this value reaches about 1 nm. Two key observations can be made which indicate that the rise of the perovskite lattice around the particle is indeed illustrating socket formation. First, the ratio between the final values of the perovskite lattice rise and particle diameter (width) is about 1/3, which is the value reported previously for the degree of immersion of exsolved particles, as measured under ambient conditons.[7] Secondly, fitting the particle growth data with models developed in the literature provides indications on particle confinement. Generally, three key factors have been previously identified in the literature to describe the rate limiting process of particle growth during exsolution: the availability or concentration of exsolvable ions in the lattice (essentially the substitution level, Eq. 1), the diffusion of the exsolvable ions (Eq. 2) to the surface and the strain associated with the formation of the particle and that of the particle-perovskite interface (Eq. 3).[27,31] In these equations d, t and τ denote particle dimension (at a given time and at equilibrium), time and time constant, respectively.

$$d_s(t) = d_{s0}\left(ln\left(1+\frac{t}{\tau_s}\right)\right)^{\frac{1}{3}} \quad \text{(Eq. 1)}$$

$$d_c(t) = d_{c0}\left(1-exp\left(-\frac{t}{\tau_r}\right)\right)^{\frac{1}{3}} \quad \text{(Eq. 2)}$$

$$d_d(t) = d_{d0}\left(\frac{t}{\tau_d}\right)^{\frac{1}{6}} \quad \text{(Eq. 3)}$$

By fitting the particle size *versus* time data obtained in our current ETEM experiment with these models, it becomes apparent that the growth of the particle size is limited by the concentration of exsolvable ions and by strain. This indicates that the particle is indeed evolving in a confined environment delimited by the perovskite lattice rising around it. Overall, the kinetic data discussed above illustrates that the genesis of the particle and of the socket are intimately linked, occurring in a concerted manner.

Another notable aspect revealed by inspection of Fig. 2c is that the location of the particle-socket does not change during the time scale of the experiment implying that the nanostructure is seemingly locked in place once formed. This seems to be additionally supported by the fact that throughout the duration of this experiment two additional particles form within nanoscale proximity of the first one but neither of these move or drift under the electron beam. This also indicates that particle-support interactions strongly dominate over particle-particle interactions. Overall, these observations explain the outstanding anchorage of exsolved particles, at relatively high temperatures of 900 ºC, which so far have only been inferred from indirect measurements, but never observed directly.

In order to probe if particle mobility becomes more prominent during the later stages of growth and when there is a higher concentration of particles or exsolvable ions available, we employ the

higher concentration sample. To facilitate simultaneous tracking of multiple particles, within a relatively narrow field of view but on different "grains", we prepared this sample as a lamella (Fig. 3a) and proceed to heat it quickly to produce multiple internal fractures (Fig. 3b).

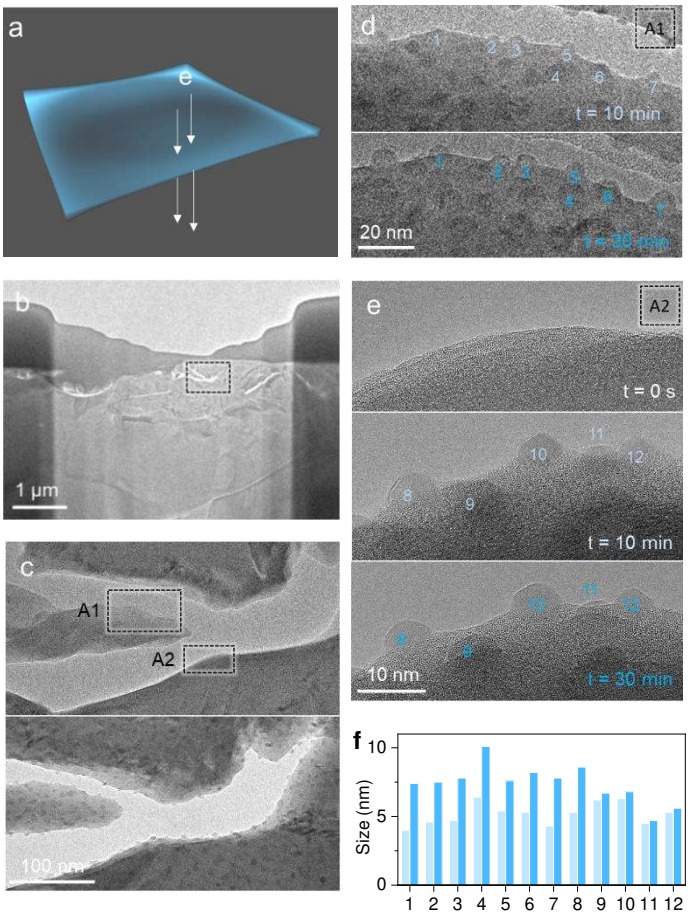

Figure 3. Monitoring particle anchorage during *in situ* growth under H_2. (a) Schematic illustration of a lamella prepared by FIB extraction from a regular sample, in a suitable orientation for electron microscopy imaging. (b) TEM of a lamella from a $La_{0.8}Ce_{0.1}Ti_{0.6}Ni_{0.4}O_3$ sample. (c) Selected area of the lamella (top) before and (bottom) after particle exsolution carried out in the ETEM under H_2 atmosphere, at 650 ºC. (d) Selected area A1 of the lamella at different times during growth, highlighting tracked particles. (e) Selected area A2 of the lamella before particle exolution and at

different times during growth, highlighting tracked particles. (f) Particle size for the tracked particles at (light blue) early growth stage and (blue) later growth stages.

We then monitor the evolution of multiple particles during the later stages of particle growth for two selected areas (Fig. 3c). Fig. 3c shows that upon exsolution, a large number of particles were formed, in nanoscale proximity of each other. Fig. 3d shows the evolution of seven tracked particles before and after 10 and 30 minutes of elapsed time. Clearly, the particles grow in size by about 40% (Fig. 3f) over this duration, but still do not appear to move across the surface, consistent with the behaviour observed during the early stages of growth. Similarly, Fig. 3e provides a closer view of tracked particles in a second area, A2, which demonstrate a similar behaviour, although their growth seems to have stabilised faster than those in area A1.

Various particle formation scenarios have been envisaged in the literature so far to explain the formation of the socket and the corresponding interface, with various degrees of supporting evidence. The generally accepted view is that the metallic nanoparticles would nucleate just under the free surface, growing to a critical size at which they would be expelled from the host lattice, while remaining partly immersed.[29] While this perspective accounts for the socket formation, nucleation within an oxide lattice has recently been shown to be unfavourable due to relatively high energy barriers arising from strain and oxide lattice reconstruction around the particle.[27,39] At the same time, this mechanism assumes metal particle transport through the perovskite lattice which is inconsistent with our current direct observations which do not show particles moving on the timescale of their growth. Our results suggest that during exsolution, particles grow epitaxially and isotropically, maintaining the same location where they initially nucleated, while the perovskite lattice concomitantly rises around it (Fig. 4a, b). As the particle grows, perhaps due to its nucleation within the surface and isotropic expansion, it pushes the perovskite lattice laterally,

forming a “volcano”-shaped socket (Fig. 4c). Over time, this volcano-like nanostructure relaxes in order to minimize surface tension (Fig. 4d), eventually approaching a more moderate shape with a subtle perovskite surface rise at the junction with the nanoparticle. Evidence of this evolution can be seen in Fig. 3e for example particles 8 and 12 and also by re-examining previous literature reports through the lens of the current observations.[24,35,40,41] Overall, the evidence presented above captures the dynamics of the exsolution process at the defining stages for developing the structural characteristics that endow exsolved particles their distinctive properties.

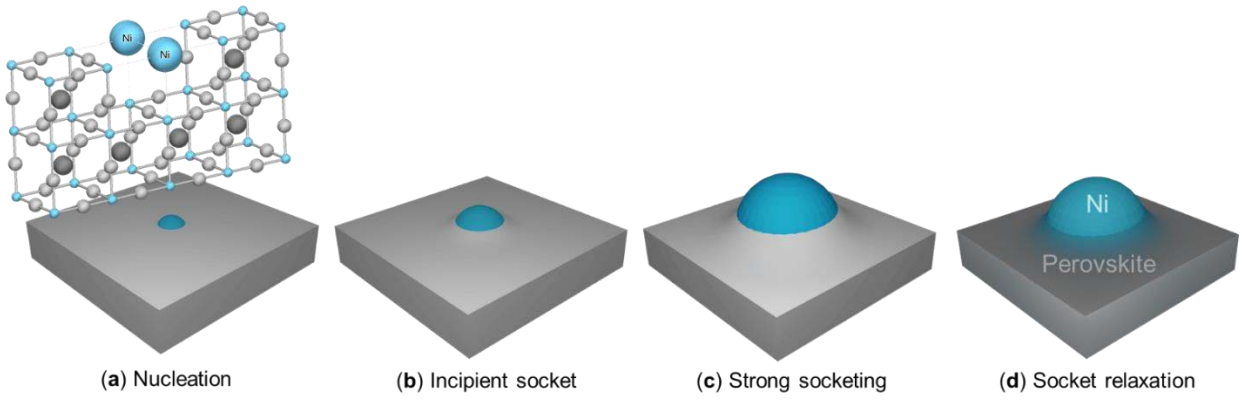

Figure 4. Schematic illustration of particle-socket genesis during exolution. (**a**) Nucleation at different length-scales depicting the particle as partly embedded within the perovskite surface as a consequence of the metal segregating out of the perovskite lattice. (**b**) As the particle grows isotropically (laterally and vertically), it pushes the perovskite lattice, lifting it slightly. (**c**) Further growth of the particle leads to a volcano-shaped nanostructure around it. (**d**) the volcano-shape interface eventually relaxes but retains confinement of the particle.

Visualising exsolution dynamics from nucleation to growth. As outlined above, the observation of the very first moments of the particle nucleation is very challenging to capture. The difficulty largely seems to reside in the tremendously fast and unpredictable process with which

this occurs. In order to slow down this process, we attempted to carry out exsolution under ETEM vacuum environment, in absence of an actively reducing gas atmosphere, at 900 ºC, for the lower substituted sample, $La_{0.43}Ca_{0.37}Ni_{0.06}Ti_{0.94}O_3$. Interestingly, such conditions were sufficient to observe extensive particle exsolution (see Fig. 5a and next section), and also enabled to us to capture the dynamics of both the nucleation and growth processes (Fig. 6).

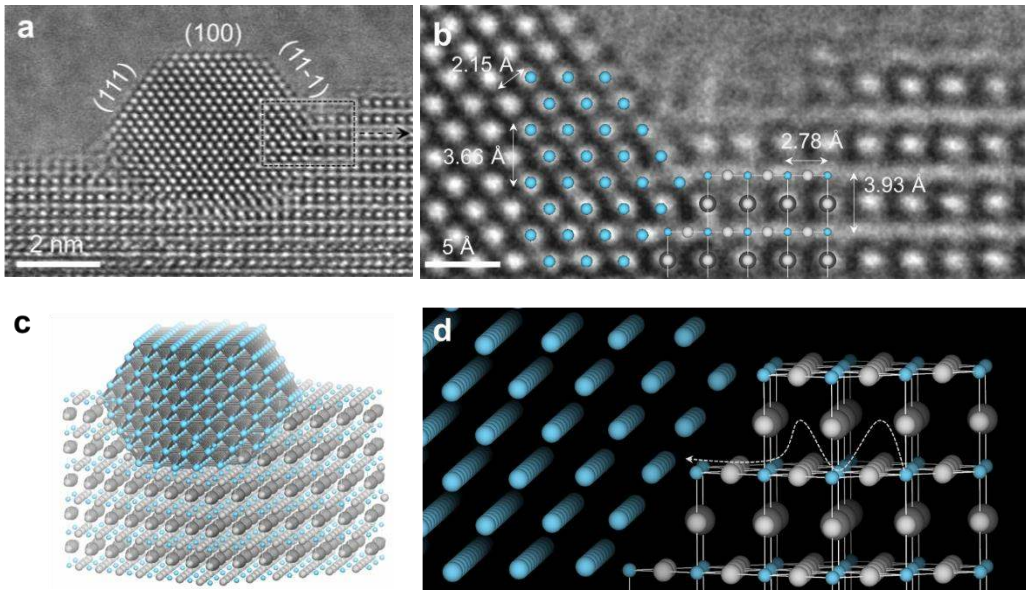

Figure 5. Particle-perovskite interface alignment. (**a**) TEM of a Ni metal nanoparticle grown under vacuum, in the ETEM, at 900 °C from $La_{0.43}Ca_{0.37}Ti_{0.94}Ni_{0.06}O_3$. (**b**) Zoom in of the particle-perovskite interface with an overlay of the Ni metal and perovskite lattices in their respective orientations, marked with the black rectangle in **a** showing the epitaxial growth. (**c**) 3D model constructed based on the crystallographic relationships highlighted in **a** and **b**. (**d**) detail of the 3D model in **c** highlighting the diffusion pathway of Ni^{2+} ions throughout the perovskite lattice.

The particles produced under high vacuum, ETEM observation conditions are still metallic Ni (based on crystal structure and lattice spacing), but strongly faceted, as shown in Fig. 5a. A closer look at these indicates that they still share strong structural similarities to those produced under H_2

atmosphere. They still appear to be partially immersed in the perovskite host lattice and also strongly epitaxial with it, as illustrated in Fig. 5a,b. The epitaxial relationship is similar to the one seen above (and in the literature[6]) for particles produced under H_2 although here the crystallographic alignment between the two lattices is strikingly precise with respect to all major directions [100], [110] and [111]. The exposed facets of the particle are (111) and (11-1) laterally and (100) parallel to the surface of the perovskite. The identified crystallographic orientation allowed us to create a 3D model of the particle which is shown in Fig. 5c,d. The orientation relationship is consistent with previous reports whereby the diffusion direction for B-site ions in perovskites is along the [110] orientation.[42,7]

Fig. 6 shows TEM snapshots of the time evolution of a nanoparticle over 15 minutes of continuous monitoring. The width and height of the particle were calculated from multiple such snapshots across the entire time range which enabled us to reveal insights into the dynamics of particle nucleation and growth during exsolution, as summarised in Fig. 7. Close inspection of the TEM images (Fig. 6) in conjunction with a plot of the particle dimensions as function of time on a logarithmic scale (Fig. 7a) reveals that nucleation occurs in a very short timescale of under 0.2 s with the particle growing to a critical size of just under 1 nm within 0.4 s. This initial ultrafast growth is followed by a hiatus where no growth occurs for a duration of about 10 s. This is then followed by a period of 10-100 s when the particle seems to display a relatively accelerated growth before reaching its apparent equilibrium size. Nonetheless, across the entire time range, particle evolution remains isotropic, growing proportionally in both height and width simultaneously (see Fig. 7b), consistent with the behaviour observed above for the particles grown under H_2 atmosphere. The outstanding spatial and temporal resolution provided by the ETEM was instrumental in revealing that interestingly, throughout the entire growth process, the growth

kinetics are not monotonic, but increase in a discrete, stepwise manner, alternating between periods of hiatus and periods of sudden growth. This "quantic" growth indicates that exsolution is a highly controlled process down to individual particle. This, together with the highly uniform patterns in which nanoparticles emerge in terms of particle size and interparticle separation, shows that exsolution is a highly controlled and discreet multiscale nano-structuring process.

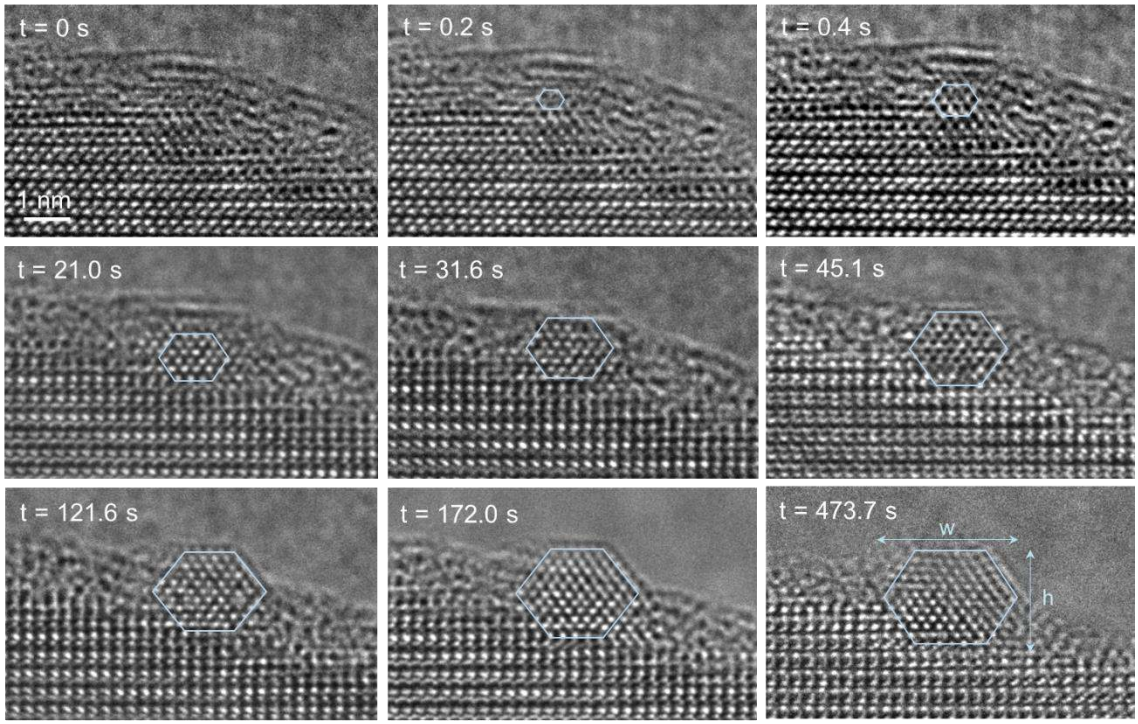

Figure 6. Direct observation of particle nucleation and growth, *in situ*, under vacuum. TEM snapshots of the exsolution of a Ni metal particle at the surface of a $La_{0.43}Ca_{0.37}Ti_{0.94}Ni_{0.06}O_3$ powder, at different times during an *in situ* ETEM reduction carried out under vacuum at 900 °C. The light blue contours highlight the growing nanoparticle.

Knowing the crystallographic orientation of the particle (Fig. 5a) and that fact that it grows isotropically enabled us to construct 3D models corresponding to the key stages of growth, as illustrated in Fig. 7c. In turn, this allowed us to estimate the number of Ni atoms contained in the

particle and therefore number of atoms exsolved at each time step; a plot of these can be seen in Fig. 7d. This kinetic data is essential in order to understand the factors that limit the exsolution process at this scale. In order to better understand this, we analyse these data with the same rate-limiting models discussed above (Eq. 1-3). Fig. 7d illustrates that the particle growth data is best described by the model where growth is limited by the availability of exsolvable ions, with the strain-limiting model being a close match. Overall, this is a surprising, yet insightful result for the design of exsolved materials. It shows that cation diffusion, which is expected to be the rate limiting step due to the relatively low diffusion of cations, does not seem to limit particle growth at this temperature. Instead, particle growth is limited by the locally available concentration of exsolvable ions and by the strain incurred due to the confined nature of exsolved particles. The depth from which ions are extracted from the perovskite to form the ~3 nm particle is plotted in Fig. 7e and is of the order of 10 nm while the relative volumes of the perovskite required for exolution and of the particle can be visualised in Fig. 7f. The depth of perovskite that needs to be depleted of exsolvable ions is considerable, as illustrated in Fig. 7f, suggesting that ions do need to travel across a few tens of perovskite unit cells to reach the surface and form the particle. The relative size between the particle size and exolution depth is consistent with the literature showing that generally for ~30 nm particles exsolution does not draw ions from further than about 100 nm.[7,8] Overall, these observations highlight the need to design exsolved materials that have grain size which scale with the desired extent of exsolution or particle size and population in order to maximise the exsolution process.

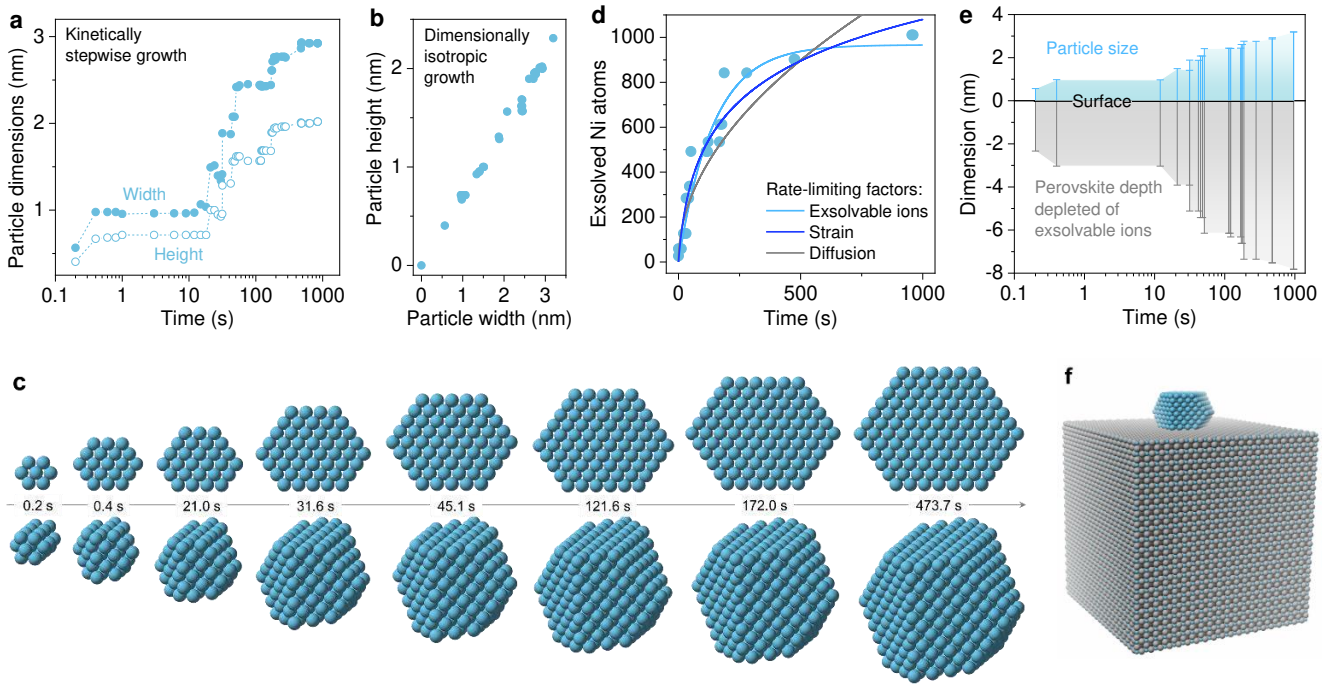

Figure 7. Atomic scale mechanistic insight into particle exsolution. (**a**) Plot of the width and height of the particle as a function of time, based on the TEM data selectively shown in Fig. 6. (**b**) Plot of the particle width vs height corresponding to the data shown in **a**. (**c**) 2D and 3D models of the time evolution of a particle during exolution, constructed based on Fig. 6. (**d**) Plot of the number of Ni metal atoms contained within the particle as a function time, together with various models describing the rate-limiting processes that govern particle growth. (**e**) Plot of the average particle size and corresponding depth within the perovskite that has been depleted of Ni^{2+} ions. (**f**) 3D model of a particle in final stages of growth and the corresponding perovskite volume required to form it.

Advanced exsolved nanostructures based on shape control and emergent heterostructures. To the best of our knowledge, all the particles produced so far by exsolution reported in the literature display quasi-spherical or ellipsoidal geometry. The same shape can be observed in the first part of our experiments illustrated by Fig. 2,3. All of these have in common the fact they are

produced under the same H_2 containing reducing atmosphere. In direct contrast to this, the particles grown under vacuum ETEM environment are distinctly faceted. Particle growth in these conditions still appears to be homogenously dispersed, much like their H_2 grown analogues occurring at different locations on the surface, an atomically flat surface or near step edges (Fig. 8a). However, it should be noted that irrespective of growth location, all particles shared identical shape and the same orientation relationship with the support, suggesting that this is an extensive phenomenon, not a local one. Furthermore, this indicates that the shape of exsolved particles may be controlled *via* the atmosphere in which exsolution is carried out. This premise was confirmed by carrying out reduction in a CO atmosphere which interestingly, produced cubic-shaped particles, as shown in Fig. 8b. Furthermore, by using slightly humidified H_2 at higher temperatures (1000 °C) another interesting effect was observed; the growth of an oxide appendage (likely La_2TiO_5) adjacent to the particles, forming heterostructures, as shown in Fig. 8c,d. This phenomenon appears to be similar to the growth of SrO nanorods adjacent to Fe particles exsolved under slightly humidified H_2,[43] although here these heterostructures seem to occur on a larger, more controlled scale.

The above results have key consequences, in how the exsolution process may be tailored. First, by controlling the nature (*e.g.* gas type) and the pO_2 of the reducing atmosphere, the shape of exsolved particles may be modified. This is very important for many catalytic processes where specific exposed facets are more desirable than others. Second by expanding the exsolution process beyond production of simple metal nanoparticles and producing coupled metal-metal oxide heterointerfaces with applications in catalysis and beyond.

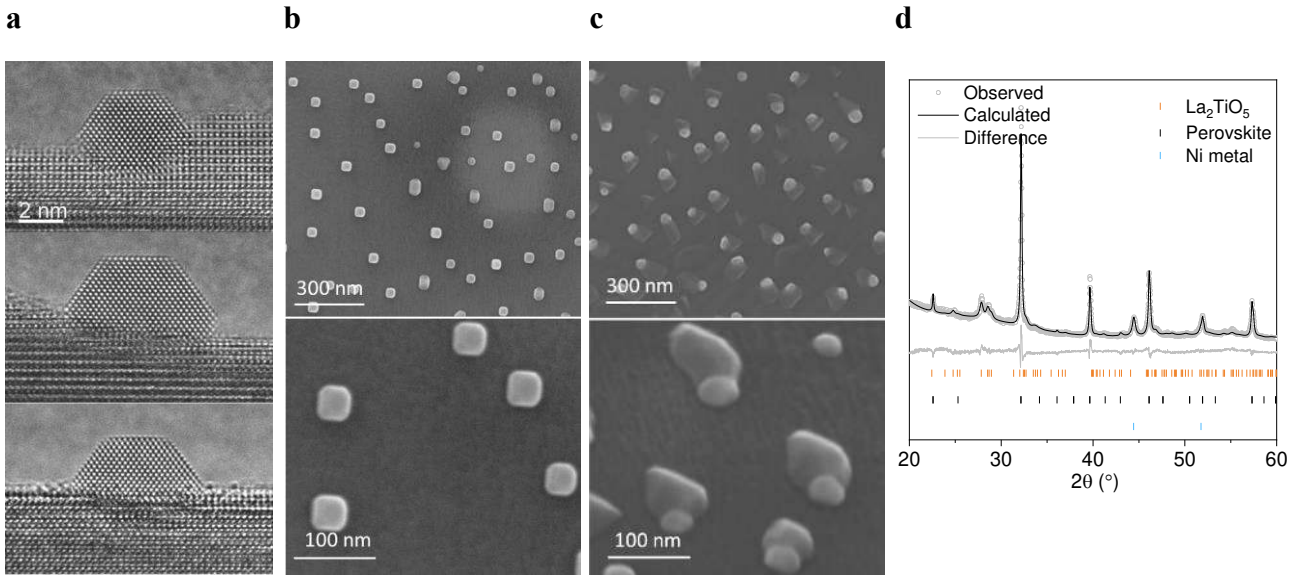

Figure 8. Advanced exsolved nanostructures based on particle shape control and heterostructures. (**a**) Faceted particles grown under vacuum, in the ETEM, at 900 ºC from $La_{0.43}Ca_{0.37}Ti_{0.94}Ni_{0.06}O_3$. (**b**) Cubic-shaped particles grown under 5% CO atmosphere at 900 ºC, for 10 h, from $La_{0.8}Ce_{0.1}Ti_{0.6}Ni_{0.4}O_3$. (**c**) Ellipsoid-shaped particles interfaced with ad-grown oxide (La_2TiO_5), under 2.5% H_2O / 5% H_2 atmosphere, at 1000 ºC, for 10 h, from $La_{0.8}Ce_{0.1}Ti_{0.6}Ni_{0.4}O_3$. (**d**) Quantitative Rietveld refinement analysis of the XRD pattern corresponding to sample **c**, showing that one mole of initial perovskite forms approximately: 0.25 mols of Ni, 0.15 mols of La_2TiO_5 and 0.6 mols of residual perovskite.

CONCLUSIONS

The present work demonstrates the use of advanced environmental transmission electron microscopy to monitor qualitatively and quantitatively the nucleation and growth of exsolved particles with ultra-high spatial and temporal resolution. These results provide powerful mechanistic insight into the atomic scale processes that underpin the formation of the particles and their highly functional interface with the perovskite lattice. By direct observation, we confirm

previous assumptions that during exsolution, particles grow epitaxially and isotropically, maintaining the same position where they initially nucleated. We observe that as the particle grows, the perovskite lattice concomitantly rises around it, forming the socket, seemingly confining and straining the particle throughout its growth. Quantitative analysis allowed us to construct 3D models of the stages of particle formation, revealing that in the defining stages of growth exsolution generally appears to be a stepwise, discrete process, from a kinetic point of view. Moreover, this also allows us to demonstrate that exsolution appears to be limited by the availability of exsolvable ions and not by their diffusion to the surface, which means that the extend of exsolution can be modified by controlling the particle size and perovskite grain or crystallite size.

Additionally, we have shown that these results enabled us to discover that the nature of the environment in which exsolution occurs (*e.g.* the gas atmosphere and pO_2) has a profound effect in dictating the shape of the exsolved particles. This could be used advantageously to control the shape of exsolved particles and expose crystal facets that could be more desirable for increasing catalytic reactivity. At the same time, the nature of the growth environment controls the formation of more advanced, dual-phase heterostructures with potentially useful physical and chemical properties and applications in catalysis and beyond.

MATERIALS AND METHODS

Perovskite oxide powders were prepared by a modified solid state synthesis described in detail previously.[6] The phase purity and crystal structure of the prepared perovskites was confirmed by room temperature XRD by using a PANalytical X'Pert Pro Multipurpose X-ray diffractometer operated in reflection mode. Rietveld refinement analysis was carried out using GSAS II. The

following parameters were gradually unlocked and refined: background (shifted Chebyshev polynomial, 3-6 terms), peak shape, unit cell parameters, atomic coordinates, site occupancies, thermal displacement parameters and microstrain. High-resolution secondary and backscattered electron images were obtained using a FEI Helios Nanolab 600 scanning electron microscope (SEM).

A cross-sectional sample (lamella) for transmission electron microscopy (TEM) analysis was made by means of standard focus ion beam (FIB) lift-out sample preparation by a FEI Quanta 3D FEG instrument SEM/FIB. Prior to FIB milling, a Pt protective layer was deposited.

An FEI TITAN ETEM G2 80–300 kV instrument equipped with an objective Cs aberration corrector was used for the observations of the catalyst (0.09 nm resolution in TEM mode and 0.136 nm STEM-HAADF mode). The ETEM can operate under gas pressure up to at 20 mbar and temperature up to under 1300 °C. The gas provider was ALPHAGAZ TM 1 Air Liquide. The microscope was also equipped with an energy dispersive X-ray (EDX) analyzer (SDD X-Max 80 m m2 from Oxford Instruments), a Gatan Imaging Filter Tridiem ERS (Gatan Instruments) and a Gatan OneView Camera. The samples were crushed in a mortar and dispersed in ethanol, the solution was ultrasonically stirred before dropping it on a MEMS chip that were then installed on DENSolutions wild fire sample holder. Crystal structures were constructed using CrystalMaker X for Windows.

AUTHOR INFORMATION

Corresponding Authors

*E-mail: dragos.neagu@newcastle.ac.uk and M.Tsampas@differ.nl

ORCID

D. Neagu: 0000-0001-7208-1055

V. Kyriakou: 0000-0002-7088-1160

C. Tang: 0000-0003-3994-9371

K. Kousi: 0000-0002-1041-8633

M.N. Tsampas: 0000-0002-4367-4457

Notes

The authors declare no competing financial interest.

ACKNOWLEDGMENTS

We thank the Consortium Lyon Saint-Etienne de Microscopie (CLYM, www.clym.fr) for its guidance in the ETEM project, which was financially supported by the CNRS, the Région Rhône-Alpes, the 'GrandLyon' and the French Ministry of Research and Higher Education. The authors acknowledge the METSA network (http://metsa.prod.lamp.cnrs.fr) for financial support. The research leading to these results has received funding by the Netherlands Organization for Scientific Research (NWO) and Syngaschem BV in the frame of from the SynCat@DIFFER program between the Dutch institute for fundamental energy research (DIFFER), Eindhoven University of Technology (TU/e) and Syngaschem BV, the European Research Council under the European Union's Seventh Framework Programme (FP/2007-2013) / ERC Grant Agreement Number 320725 and from the EPSRC *via* grants EP/P007767/1, EP/P024807/1 and EP/R023921/1. We also thank the European Synchrotron Radiation Facility (ESRF) and Dr. Catherine Dejoie the X-ray synchrotron data.

Raw data supporting the figures of this publication are available at doi: 10.25405/data.ncl.8859443.

REFERENCES

(1) Vernoux, P.; Lizarraga, L.; Tsampas, M. N.; Sapountzi, F. M.; De Lucas-Consuegra, A.; Valverde, J.-L.; Souentie, S.; Vayenas, C. G.; Tsiplakides, D.; Balomenou, S.; Baranova, E. A. Ionically Conducting Ceramics as Active Catalyst Supports. *Chem. Rev.* **2013**, *113*, 8192–8260..

(2) Irvine, J. T. S.; Neagu, D.; Verbraeken, M. C.; Chatzichristodoulou, C.; Graves, C.; Mogensen, M. B. Evolution of the Electrochemical Interface in High-Temperature Fuel Cells and Electrolysers. *Nat. Energy* **2016**, *1*, 15014.

(3) Liu, L.; Corma, A. Metal Catalysts for Heterogeneous Catalysis: From Single Atoms to Nanoclusters and Nanoparticles. *Chem. Rev.* **2018**, *118*, 4981–5079.

(4) Takehira, K. Highly Dispersed and Stable Supported Metal Catalysts Prepared by Solid Phase Crystallization Method. *Catal. Surv. Asia* **2002**, *6*, 19–32.

(5) Nishihata, Y.; Mizuki, J.; Akao, T.; Tanaka, H.; Uenishi, M.; Kimura, M.; Okamoto, T.; Hamada, N. Self-Regeneration of a Pd-Perovskite Catalyst for Automotive Emissions Control. *Nature* **2002**, *418*, 164–167.

(6) Neagu, D.; Tsekouras, G.; Miller, D. N.; Ménard, H.; Irvine, J. T. S. *In Situ* Growth of Nanoparticles through Control of Non-Stoichiometry. *Nat Chem* **2013**, *5*, 916–923.

(7) Neagu, D.; Oh, T.-S.; Miller, D. N.; Ménard, H.; Bukhari, S. M.; Gamble, S. R.; Gorte, R. J.; Vohs, J. M.; Irvine, J. T. S. Nano-Socketed Nickel Particles with Enhanced Coking Resistance Grown *In Situ* by Redox Exsolution. *Nat. Commun.* **2015**, *6*, 8120.

(8) Neagu, D.; Papaioannou, E. I.; Ramli, W. K. W.; Miller, D. N.; Murdoch, B. J.; Ménard, H.; Umar, A.; Barlow, A. J.; Cumpson, P. J.; Irvine, J. T. S.; Metcalfe, I. S. Demonstration of Chemistry at a Point through Restructuring and Catalytic Activation at Anchored Nanoparticles. *Nat. Commun.***2017**, *8*, 1855.

(9) Madsen, B. D.; Kobsiriphat, W.; Wang, Y.; Marks, L. D.; Barnett, S. SOFC Anode Performance Enhancement through Precipitation of Nanoscale Catalysts. *ECS Trans.* **2007**, *7*, 1339–1348.

(10) Zhu, Y.; Zhou, W.; Ran, R.; Chen, Y.; Shao, Z.; Liu, M. Promotion of Oxygen Reduction by Exsolved Silver Nanoparticles on a Perovskite Scaffold for Low-Temperature Solid Oxide Fuel Cells. *Nano Lett.* **2016**, *16*, 512–518.

(11) Hou, N.; Yao, T.; Li, P.; Yao, X.; Gan, T.; Fan, L.; Wang, J.; Zhi, X.; Zhao, Y.; Li, Y. A-Site Ordered Double Perovskite with *In Situ* Exsolved Core–Shell Nanoparticles as Anode for Solid Oxide Fuel Cells. *ACS Appl. Mater. Interfaces* **2019,** *11*, 6995-7005.

(12) Joo, S.; Kwon, O.; Kim, K.; Kim, S.; Kim, H.; Shin, J.; Jeong, H. Y.; Sengodan, S.; Han, J. W.; Kim, G. Cation-Swapped Homogeneous Nanoparticles in Perovskite Oxides for High Power Density. *Nat. Commun.* **2019**, *10*, 697.

(13) Zhu, T.; Troiani, H. E.; Mogni, L. V.; Han, M.; Barnett, S. A. Ni-Substituted $Sr(Ti,Fe)O_3$ SOFC Anodes: Achieving High Performance *via* Metal Alloy Nanoparticle Exsolution. *Joule* **2018**, *2*, 478–496.

(14) Tsekouras, G.; Neagu, D.; Irvine, J. T. S. Step-Change in High Temperature Steam Electrolysis Performance of Perovskite Oxide Cathodes with Exsolution of B-Site Dopants. *Energy Environ. Sci.* **2013**, *6*, 256–266.

(15) Myung, J.; Neagu, D.; Miller, D. N.; Irvine, J. T. S. Switching on Electrocatalytic Activity in Solid Oxide Cells. *Nature* **2016**, *537*, 528–531.

(16) Zhu, C.; Hou, S.; Hu, X.; Lu, J.; Chen, F.; Xie, K. Electrochemical Conversion of Methane to Ethylene in a Solid Oxide Electrolyzer. *Nat. Commun.* **2019**, *10*, 1173.

(17) Wang, R.; Dogdibegovic, E.; Lau, G. Y.; Tucker, M. C. Metal-Supported Solid Oxide Electrolysis Cell (MS-SOEC) With Significantly Enhanced Catalysis. *Energy Technol-Gen* **2019**, *7*, 1801154..

(18) Liu, S.; Liu, Q.; Luo, J.-L. Highly Stable and Efficient Catalyst with *In Situ* Exsolved Fe–Ni Alloy Nanospheres Socketed on an Oxygen Deficient Perovskite for Direct CO_2 Electrolysis. *ACS Catal.* **2016**, *6*, 6219–6228.

(19) Kyriakou, V.; Neagu, D.; Papaioannou, E. I.; Metcalfe, I. S.; Sanden, M.; Tsampas, M. N. Co-Electrolysis of H_2O and CO_2 on Exsolved Ni Nanoparticles for Efficient Syngas Generation at Controllable H_2/CO Ratios. *Appl. Catal. B-Environ.* **2019,** *243*, 490-501.

(20) Hosseini, D.; Donat, F.; Abdala, P. M.; Kim, S. M.; Kierzkowska, A. M.; Müller, C. R. Reversible Exsolution of Dopant Improves the Performance of $Ca_2Fe_2O_5$ for Chemical Looping Hydrogen Production. *ACS Appl. Mater. Interfaces* **2019**, *11*, 18276-18284.

(21) Dimitrakopoulos, G.; Ghoniem, A. F.; Yildiz, B. *In Situ* Catalyst Exsolution on Perovskite Oxides for the Production of CO and Synthesis Gas in Ceramic Membrane Reactors. *Sustainable Energy Fuels* **2019**, *3*, 2347-2355.

(22) Yan, B.; Wu, Q.; Cen, J.; Timoshenko, J.; Frenkel, A. I.; Su, D.; Chen, X.; Parise, J. B.; Stach, E.; Orlov, A.; Chen, J. G. Highly Active Subnanometer Rh Clusters Derived from Rh-Doped $SrTiO_3$ for CO_2 Reduction. *Appl. Catal. B-Environ.* **2018**, *237*, 1003-1011.

(23) Sun, Y.; Yang, Y.; Chen, J.; Li, M.; Zhang, Y.; Li, J.; Hua, B.; Luo, J.-L. Toward Rational Photocatalyst Design: A New Formation Strategy of Co-Catalyst/Semiconductor Heterostructure *via In Situ* Exsolution. *Chem. Commun.* **2018**, *54*, 1505-1508.

(24) Thalinger, R.; Gocyla, M.; Heggen, M.; Dunin-Borkowski, R.; Grünbacher, M.; Stöger-Pollach, M.; Schmidmair, D.; Klötzer, B.; Penner, S. Ni–Perovskite Interaction and Its Structural and Catalytic Consequences in Methane Steam Reforming and Methanation Reactions. *J. Catal.* **2016**, *337*, 26–35.

(25) Zubenko, D.; Singh, S.; Rosen, B. A. Exsolution of Re-Alloy Catalysts with Enhanced Stability for Methane Dry Reforming. *Appl. Catal. B-Environ.* **2017**, *209*, 711–719.

(26) Wang, Z.; Cheng, Y.; Shao, X.; Veder, J.-P.; Hu, X.; Ma, Y.; Wang, J.; Xie, K.; Dong, D.; Ping Jiang, S.; Parkinson, G. ; Buckley, C. ; Li, C-Z. Nanocatalysts Anchored on Nanofiber Support for High Syngas Production *via* Methane Partial Oxidation. *Appl. Catal. A-Gen.* **2018**, *565*, 119–126.

(27) Gao, Y.; Chen, D.; Saccoccio, M.; Lu, Z.; Ciucci, F. From Material Design to Mechanism Study: Nanoscale Ni Exsolution on a Highly Active A-Site Deficient Anode Material for Solid Oxide Fuel Cells. *Nano Energy* **2016**, *27*, 499–508.

(28) Jo, Y.-R.; Koo, B.; Seo, M.-J.; Kim, J. K.; Lee, S.; Kim, K.; Han, J. W.; Jung, W.; Kim, B.-J. Growth Kinetics of Individual Co Particles Ex-Solved on $SrTi_{0.75}Co_{0.25}O_{3-\delta}$ Polycrystalline Perovskite Thin Films. *J. Am. Chem. Soc.* **2019**, *141*, 6690-6697.

(29) Oh, T.-S.; Rahani, E. K.; Neagu, D.; Irvine, J. T. S.; Shenoy, V. B.; Gorte, R. J.; Vohs, J. M. Evidence and Model for Strain-Driven Release of Metal Nanocatalysts from Perovskites during Exsolution. *J. Phys. Chem. Lett.* **2015**, *6*, 5106–5110.

(30) Götsch, T.; Schlicker, L.; F. Bekheet, M.; Doran, A.; Grünbacher, M.; Praty, C.; Tada, M.; Matsui, H.; Ishiguro, N.; Gurlo, A.; Klötzer, B.; Penner, S. Structural Investigations of $La_{0.6}Sr_{0.4}FeO_{3-\delta}$ under Reducing Conditions: Kinetic and Thermodynamic Limitations for Phase Transformations and Iron Exsolution Phenomena. *RSC Adv.* **2018**, *8*, 3120–3131.

(31) Gao, Y.; Lu, Z.; You, T. L.; Wang, J.; Xie, L.; He, J.; Ciucci, F. Energetics of Nanoparticle Exsolution from Perovskite Oxides. *J. Phys. Chem. Lett.* **2018**, *9*, 3772-3778.

(32) Kim, K. J.; Han, H.; Defferriere, T.; Yoon, D.; Na, S.; Kim, S. J.; Dayaghi, A. M.; Son, J.; Oh, T.-S.; Jang, H. M.; Choi, J. M. Facet-Dependent *In Situ* Growth of Nanoparticles in Epitaxial Thin Films: The Role of Interfacial Energy. *J. Am. Chem. Soc.* **2019**, *141*, 7509-7517.

(33) Singh, S.; Prestat, E.; Huang, L.-F.; Rondinelli, J. M.; Haigh, S. J.; Rosen, B. A. Role of 2D and 3D Defects on the Reduction of LaNiO 3 Nanoparticles for Catalysis. *Sci. Rep.-UK* **2017**, *7*, 10080.

(34) Kwon, O.; Sengodan, S.; Kim, K.; Kim, G.; Jeong, H. Y.; Shin, J.; Ju, Y.-W.; Han, J. W.; Kim, G. Exsolution Trends and Co-Segregation Aspects of Self-Grown Catalyst Nanoparticles in Perovskites. *Nat. Commun.* **2017**, *8*, 15967.

(35) Han, H.; Park, J.; Nam, S. Y.; Kim, K. J.; Choi, G. M.; Parkin, S. S. P.; Jang, H. M.; Irvine, J. T. S. Lattice Strain-Enhanced Exsolution of Nanoparticles in Thin Films. *Nat. Commun.* **2019**, *10*, 1471.

(36) Jinschek, J. R. Advances in the Environmental Transmission Electron Microscope (ETEM) for Nanoscale *In Situ* Studies of Gas–Solid Interactions. *Chem. Commun.* **2014**, *50*, 2696–2706.

(37) Serve, A.; Epicier, T.; Aouine, M.; Cadete Santos Aires, F. J.; Obeid, E.; Tsampas, M.; Pajot, K.; Vernoux, P. Investigations of Soot Combustion on Yttria-Stabilized Zirconia by Environmental Transmission Electron Microscopy (ETEM). *Appl. Catal. A-Gen.* **2015**, *504*, 74–80.

(38) Epicier, T.; Aouine, M.; Aires, F. J. C. S.; Massin, L.; Gélin, P. Experimental Evidence for the Existence of an Iridium Sesquioxide Metastable Phase during ETEM Studies of Methane Steam Reforming on an Ir/$Ce_{0.9}Gd_{0.9}O_{2-x}$ Catalyst. *Microsc. Microanal.* **2018**, *24*, 1648–1649.

(39) Oh, T.-S.; Rahani, E. K.; Neagu, D.; Irvine, J. T. S.; Shenoy, V. B.; Gorte, R. J.; Vohs, J. M. Evidence and Model for Strain-Driven Release of Metal Nanocatalysts from Perovskites during Exsolution. *J. Phys. Chem. Lett.* **2015**, *6*, 5106–5110.

(40) Lv, H.; Lin, L.; Zhang, X.; Gao, D.; Song, Y.; Zhou, Y.; Liu, Q.; Wang, G.; Bao, X. *In Situ* Exsolved FeNi3 Nanoparticles on Nickel Doped $Sr_2Fe_{1.5}Mo_{0.5}O_{6-\delta}$ Perovskite for Efficient Electrochemical CO_2 Reduction Reaction. *J. Mater. Chem. A* **2019**, *7*, 11967–11975.

(41) Chen, Y.; Li, H.; Wang, J.; Du, Y.; Xi, S.; Sun, Y.; Sherburne, M.; Ager, J. W.; Fisher, A. C.; Xu, Z. J. Exceptionally Active Iridium Evolved from a Pseudo-Cubic Perovskite for Oxygen Evolution in Acid. *Nat. Commun.* **2019**, *10*, 572.

(42) De Souza, R. A.; Islam, M. S.; Ivers-Tiffée, E. Formation and Migration of Cation Defects in the Perovskite Oxide $LaMnO_3$. *J. Mat. Chem.* **1999**, *9*, 1621–1627.

(43) Thalinger, R.; Gocyla, M.; Heggen, M.; Klötzer, B.; Penner, S. Exsolution of Fe and SrO Nanorods and Nanoparticles from Lanthanum Strontium Ferrite $La_{0.6}Sr_{0.4}FeO_{3-\delta}$ Materials by Hydrogen Reduction. *J. Phys. Chem. C* **2015**, *119*, 22050–22056.

TABLE OF CONTENT